# Numerical simulation of flow around a circular cylinder having porous surface

Hiroshi Naito and Koji Fukagata

---

---

# Numerical simulation of flow around a circular cylinder having porous surface

Hiroshi Naito and Koji Fukagata
*Department of Mechanical Engineering, Keio University, Hiyoshi 3-14-1, Kohoku-ku, Yokohama 223-8522, Japan*

Flow around a circular cylinder having porous surface is studied numerically by means of direct numerical simulation and large eddy simulation. The flow in the porous media is represented by a spatially averaged model. First, the properties of the most effective porous media are found from a preliminary two-dimensional parametric test. Subsequently, the dependency of flow modification on the Reynolds number ($Re = 100$, 1000, 3900, and $1.0 \times 10^5$) and the porous layer thickness is investigated in detail. It is found that the porous surface works to suppress the velocity and pressure fluctuations and such effect is more significant at higher Reynolds number. In particular, the vortex shedding is found to be completely suppressed at $Re = 1.0 \times 10^5$. The mechanism of flow modification is explained by slip velocity and energy dissipation process. © *2012 American Institute of Physics*. [http://dx.doi.org/10.1063/1.4767534]

## I. INTRODUCTION

Control of flow around a bluff body has attracted much attention for the mitigation of environmental impact due to various industrial applications such as automobiles, airplanes, and buildings.[1] While active control methods have potentially larger effects, passive control methods have a merit that they can more easily be implemented in practical applications.

Recently, Sueki *et al.*[2] studied the control effect of porous media on the flow around a circular cylinder aiming at noise reduction of the pantograph used for bullet trains. They achieved significant noise reduction in their wind tunnel experiment. The PIV measurement at $Re = 1.3 \times 10^5$ reveals that the shear layer above the porous surface can completely be stabilized as shown in Fig. 1. Although the mechanism of flow stabilization is not always clear, their results at least suggest that the porous medium is an effective passive control device for the suppression of vortex shedding.

Toward the use of porous media in industrial applications, one should further accumulate the knowledge about its effect on the flow, including the dependency to various design parameters and the detailed mechanism of flow modification.

Bruneau and Mortazavi[3] investigated the effect of porous media on flows around a square cylinder by means of two-dimensional numerical simulation. The Reynolds number was $Re = 3000$ and 30 000. They assumed that the top and bottom layers of the square cylinder were made of porous material. It was found that the drag, the lift fluctuation, and the global enstrophy were reduced as compared to the case of solid cylinder.

Bruneau and Mortazavi[4] also studied the effect of porous media on flows around a circular cylinder at the same Reynolds numbers, i.e., $Re = 3000$ and 30 000. They assumed porous media of a uniform thickness around a circular cylinder and obtained reduction of lift force fluctuation and global enstrophy. Their computation, however, is two-dimensional despite that three-dimensionality should be taken into account at such high Reynolds numbers. In fact, the Reynolds number assumed in Bruneau and Mortazavi ($Re = 30\,000$) is relatively close to that in Sueki's experiment ($Re = 10^5$), but the resultant flow modification observed in these two are quite different. Thus, it is necessary to revisit this flow by properly taking into account the three-dimensionality effects.

In the present study, we investigate the flow around a circular cylinder having a porous surface by means of direct numerical simulation (DNS) and large eddy simulation (LES). First, we perform a
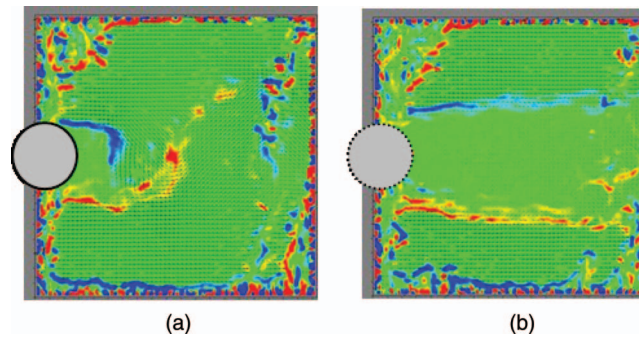
**24**, 117102-1

FIG. 1. Vorticity field obtained by PIV of Sueki *et al.*[2]: (a) solid surface case; (b) porous surface case. Reprinted with permission from K. Sueki, T. Takaishi, and M. Ikeda, Fluid Dyn. Res. **42**, 015004 (2010). Copyright 2010 IOP Publishing.

parametric test for two-dimensional (2D) flow at the Reynolds number of $Re = 1000$. Subsequently, three-dimensional (3D) DNS is performed at $Re = 1000$ and details of flow modification are analyzed. Furthermore, numerical simulations are performed also at different Reynolds numbers, $Re = 100$ (2D), 3900 (LES), and $1.0 \times 10^5$ (LES) in order to investigate the Reynolds number dependency.

## II. NUMERICAL MODEL

We assume a circular cylinder in a uniform flow, as shown in Fig. 2. The cylinder is assumed to have a porous surface of uniform thickness and uniform permeability. The governing equations for the flow outside the cylinder are the incompressible continuity and Navier-Stokes equations, i.e.,

$$\nabla \cdot \boldsymbol{u} = 0, \tag{1}$$

$$\frac{\partial \boldsymbol{u}}{\partial t} + \nabla \cdot (\boldsymbol{u}\boldsymbol{u}) = -\nabla p + \frac{1}{Re} \nabla^2 \boldsymbol{u}. \tag{2}$$

The equations are made dimensionless by using the fluid density $\rho$, the free-stream velocity $U_\infty$, and the cylinder diameter $D$; the Reynolds number is defined by $Re = \rho U_\infty D / \mu$, where $\mu$ is the dynamic viscosity.

Various methods have been proposed for the computation of flow in porous media:

1. Direct method, in which every complex geometry of porous media is resolved.[5]
2. Method of boundary condition, which uses an artificial boundary condition mimicking the effect of porous surface.[6]
3. Macroscopic flow model, which uses a volume-averaged equation in the porous media.[3]

The first method is considered most accurate, but not suited for examining the effects of various parameters on the flow due to its relatively high computational cost. The second method cannot be used in the present study since the relationship between the boundary condition and the flow information outside the porous layer is unknown. Therefore, we adopt the last method in the present study.
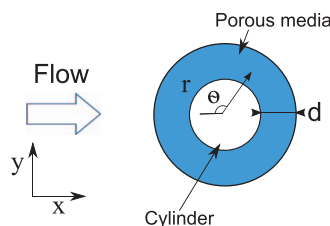


FIG. 2. Flow configuration.

In contrast to the Brinkman-Navier-Stokes equation used by Bruneau and Mortazavi,[3,4] we use the macroscopic momentum equation by Hsu and Cheng,[7] i.e.,

$$\frac{\partial \langle \boldsymbol{u} \rangle}{\partial t} + \nabla \cdot \left( \frac{\langle \boldsymbol{u} \rangle \langle \boldsymbol{u} \rangle}{\phi} \right) = -\nabla \langle p \rangle + \frac{1}{Re} \nabla^2 \langle \boldsymbol{u} \rangle + \boldsymbol{K}, \tag{3}$$

where $\langle \cdot \rangle$ denotes the macroscopic velocity inside the porous media and $\boldsymbol{K}$ is the internal frictional drag given by

$$\boldsymbol{K} = -\frac{\phi}{ReDa} \langle \boldsymbol{u} \rangle - \frac{b}{\sqrt{a}} \frac{1}{\sqrt{Da}} \frac{\langle \boldsymbol{u} \rangle |\langle \boldsymbol{u} \rangle|}{\sqrt{\phi}}. \tag{4}$$

Equation (3) is derived under the assumption that the porous medium is made of mono-dispersed spheric particles. With this assumption, the frictional force inside the porous medium is modeled by accounting for Oseen's correction. The Darcy number $Da = k/D^2$ is the permeability $k$ made dimensionless by using the cylinder diameter $D$. The permeability is related to the porosity $\phi$ and the particle diameter $d_p$ by

$$k = \frac{\phi^3 d_p^2}{a(1 - \phi)^2}, \tag{5}$$

where $a$ and $b$ are the Ergun constants. Although these constants vary slightly with porosity and structure of porous media, we assume these values to be $a = 150$ and $b = 1.75$ as obtained by Ergun.[8]

The Brinkman-Navier-Stokes equation used in the previous studies[3,4] is a classical model: the shear structure inside the porous media is neglected. In contrast, the model used in the present study includes such effect in its derivation. Throughout the present study, the surrounding porous medium is assumed to have uniform thickness $d$, permeability $k$, and porosity $\phi$. Two different thicknesses are considered: 20% and 50% of the cylinder radius (i.e., $d = 0.2\,R$ and $d = 0.5\,R$).

As shown in Table I, different methods, i.e., DNS, LES with the dynamic Smagorinsky model (DSM),[9,10] and LES with the constant Smagorinsky model (CSM),[11] are used depending on the Reynolds number. DNS may always be the best choice if the computer resource allows. For the present purpose, however, DNS also at higher Reynolds numbers is disproportionately heavy. Therefore, we adopted LES at higher Reynolds numbers: DSM at $Re = 3900$ and CSM at $Re = 1.0 \times 10^5$. Although the better choice of subgrid-scale (SGS) model may be DSM, CSM was used at $Re = 1.0 \times 10^5$ in order to save the computational cost by considering the finding by Breuer[12] that the superiority of DSM over CSM is not clear at $Re \simeq 10^5$.

The simulation code is based on the DNS code for a turbulent pipe flow of Fukagata and Kasagi[13] and adapted here to the flow around a cylinder. For low Reynolds number cases ($Re = 100$, 1000, and

TABLE I. Number of computational cells used in the present simulations.

| Reynolds number (method) | Surface | $N_r \times N_\theta \times N_z$ |
|---|---|---|
| $Re = 100$ (2D) | Solid | $220 \times 256 \times 1$ |
|  | Porous $d = 0.2R$ | $230 \times 256 \times 1$ |
|  | Porous $d = 0.5R$ | $245 \times 256 \times 1$ |
| $Re = 1000$ (3D, DNS) | Solid | $220 \times 256 \times 64$ |
|  | Porous $d = 0.2R$ | $230 \times 256 \times 64$ |
|  | Porous $d = 0.5R$ | $245 \times 256 \times 64$ |
| $Re = 3900$ (LES) | Solid | $200 \times 256 \times 64$ |
|  | Porous $d = 0.2R$ | $210 \times 256 \times 64$ |
|  | Porous $d = 0.5R$ | $225 \times 256 \times 64$ |
| $Re = 1.0 \times 10^5$ (LES) | Solid | $300 \times 512 \times 64$ |
|  | Porous $d = 0.2R$ | $375 \times 512 \times 64$ |
|  | Porous $d = 0.5R$ | $425 \times 512 \times 64$ |

TABLE II. Computational conditions.

| Reynolds number (method) | $L_r/D$ | $L_z/D$ | $\Delta r_{min}/D$ | $\Delta z/D$ | $r_{i+1}/r_i$ | $\eta_k/D$ |
|---|---|---|---|---|---|---|
| $Re = 100$ (2D) | 70 | . . . | $1.0 \times 10^{-2}$ | . . . | 1.019 | . . . |
| $Re = 1000$ (3D, DNS) | 70 | $2\pi$ | $1.0 \times 10^{-2}$ | $1.0 \times 10^{-1}$ | 1.019 | $1.27 \times 10^{-2}$ |
| $Re = 3900$ (LES) | 30 | $\pi$ | $1.5 \times 10^{-3}$ | $5.0 \times 10^{-2}$ | 1.029 | $2.88 \times 10^{-3}$ |
| $Re = 1.0 \times 10^5$ (LES) | 30 | 2 | $5.0 \times 10^{-4}$ | $3.0 \times 10^{-2}$ | 1.022 | $3.24 \times 10^{-4}$ |

3900), the energy-conservative finite difference method on the cylindrical coordinate system[13] is used for the spatial discretization. In the highest Reynolds number case ($Re = 1.0 \times 10^5$), however, the QUICK scheme[14] is used for the advection term to avoid artificial transition due to dispersion error. As for temporal integration, the low-storage third order Runge-Kutta/Crank-Nicolson (RK3/CN) scheme[15] is used with a higher-order fractional step method for the velocity-pressure coupling.[16] The pressure Poisson equation is solved by using the fast Fourier transform (FFT) in the azimuthal ($\theta$) and axial ($z$) directions and the tridiagonal matrix algorithm (TDMA) in the radial ($r$) direction. A uniform velocity, $U_\infty$, is imposed at the inlet boundary ($0 \leq |\theta| \leq \frac{3}{4}\pi$), and the convective velocity condition is used at the outlet boundary ($\frac{3}{4}\pi \leq |\theta| \leq \pi$).

The number of computational cells used is shown in Table I. The number in the radial direction is increased in the porous cases simply because the resolution in the pure fluid region is kept constant and the grid is extended inside the porous region. The size of computational domain, the size of computational cells, and the Kolmogorov length scale computed from the obtained velocity fields are summarized in Table II. Although, at $Re = 1000$ (DNS), the spanwise cell size is about 8 times larger than the Kolmogolov scale, we have confirmed that the cell size is sufficiently small to reproduce the statistics we focus on here: for instance, change in the mean drag coefficient $\overline{C_D}$ in the solid case was less than 1% when $\Delta z$ was reduced to half. The grid geometry in the solid case at $Re = 100$ and 1000 is shown in Fig. 3. Figure 3(a) represents whole computational domain, and Fig. 3(b) shows its zoom up view near the cylinder.

The simulation is initiated with a symmetric potential velocity distribution with small perturbations superimposed on it. The statistics are accumulated after the flow reaches a statistically steady state.

The present simulation is validated by comparing the major mean flow properties with the literature.[17–26] The time averaged drag coefficient $\overline{C_D}$, the root-mean-square (RMS) of lift coefficient $C'_L$, the Strouhal number $St$, and the base pressure $C_{pb}$ are compared in Table III. The present
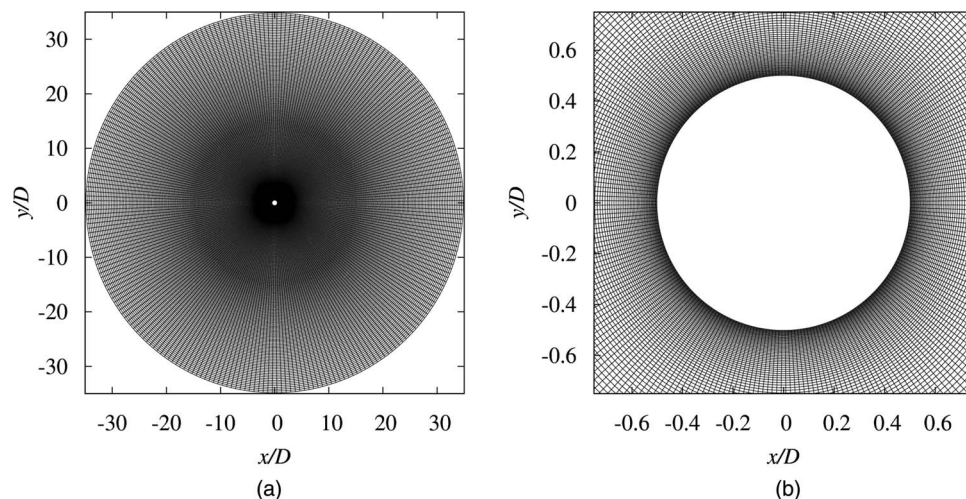


FIG. 3. Grid geometry (solid surface case at $Re = 100$ and 1000): (a) whole region; (b) near the cylinder.

TABLE III. Computed flow properties.

|  | $\overline{C_D}$ | $C_L'$ | $S_t$ | $-C_{pb}$ |
|---|---|---|---|---|
| $Re = 100$ |  |  |  |  |
| Present | 1.33 | 0.23 | 0.165 | 0.72 |
| Reference | 1.34[a] | 0.23[b] | 0.165[c] | 0.74[a, d] |
| $Re = 1000$ |  |  |  |  |
| Present (3D) | 1.09 | 0.21 | 0.21 | 0.92 |
| Reference | 1.20[e], 1.52[a] | 0.21[c, e] | 0.21[c] | 0.75[f], 0.81[d], 1.12[e], 1.69[a] |
| $Re = 3900$ |  |  |  |  |
| Present | 1.07 | 0.25 | 0.21 | 1.02 |
| Reference | 1.04[g] | 0.27[h] | 0.21[c, g] | 0.80[f], 0.87[i], 0.94[g] |
| $Re = 1.0 \times 10^5$ |  |  |  |  |
| Present | 1.46 | 0.99 | 0.183 | 1.73 |
| Reference | 1.21[j] | 0.29[j], 0.73[k] | 0.185[c], 0.20[j, k] | 1.35[i], 1.57[k] |

[a]Reference 17     [e]Reference 21     [i]Reference 25
[b]Reference 18     [f]Reference 22     [j]Reference 26
[c]Reference 19     [g]Reference 23     [k]Reference 27
[d]Reference 20     [h]Reference 24

results at $Re = 100$–3900 are in fair agreement with the literature. One can notice that numerical simulations (Henderson[17] and Henderson and Karniadakis[21] at $Re = 1000$, Kravchenko and Moin[23] at $Re = 3900$, and the present one), tend to give larger values of $-C_{pb}$ than those in experiments (Williamson and Roshko[20] and Gerrard[22] at $Re = 1000$, Williamson and Roshko[20] and Norberg[25] at $Re = 3900$), which are consistent among different experiments. Although totally unclear, this difference may be due to tiny imperfections still remaining in numerical simulations (e.g., grid resolution or computational domain size), that in experiments (e.g., free-stream turbulence or surface roughness), or both. At $Re = 1.0 \times 10^5$, the Strouhal number $St$ is in good agreement with the literature, but difference amounts to about 20% in $\overline{C_D}$, $C_L'$, and $C_{pb}$. A possible reason for this difference is the overestimation of the subgrid scale dissipation in the present LES.

The present numerical simulations were performed on a single core of Intel Core i7-960 (3.2 GHz) processor. The physical time required for simulating one non-dimensional time, i.e., $D/U_\infty$, is 15 s in $Re = 100$ and $Re = 1000$ (2D) cases, 1000 s in $Re = 1000$ (3D) case, and about $1.5 \times 10^4$ s in $Re = 3900$ and $Re = 1.0 \times 10^5$ cases. The relatively longer computational time taken for the $Re = 3900$ case is due to the computation time required for the dynamic procedure.

## III. PARAMETRIC STUDY

First, we present the results of parametric study for finding the effective porous media properties. According to Eqs. (3)–(5), two out of three parameters, i.e., $\phi$, $k$ (or $Da$), and $d_p$, are independent. Here, we chose $Da$ and $\phi$ as the parameters to be varied. Note that changing $\phi$ under a given $Da$ is equivalent to changing $d_p$. The parametric study is performed by two-dimensional simulation at $Re = 1000$ in order to save computational cost. There are many parameters involved in the present problem and it is impossible to cover all the combinations. Thus, we basically assume the values similar to those used in the experiment.[2] In total, 446 cases are simulated in the ranges of $1.0 \times 10^{-3} \leq Da \leq 1.0$ and $0.8 \leq \phi \leq 0.95$. Although two porous layer thicknesses of $d = 0.2R$ and $d = 0.5R$ are examined, here we present only the results of $d = 0.5R$ cases, in which the effect of porous layer was clearer.

The mean drag coefficient $\overline{C_D}$ and the RMS lift coefficient $C_L'$ are computed as

$$\overline{C_D} = \frac{\overline{F_x}}{\frac{1}{2}\rho U_\infty^2 D L_z}, \qquad C_L' = \frac{\sqrt{(F_y')^2}}{\frac{1}{2}\rho U_\infty^2 D L_z}, \tag{6}$$
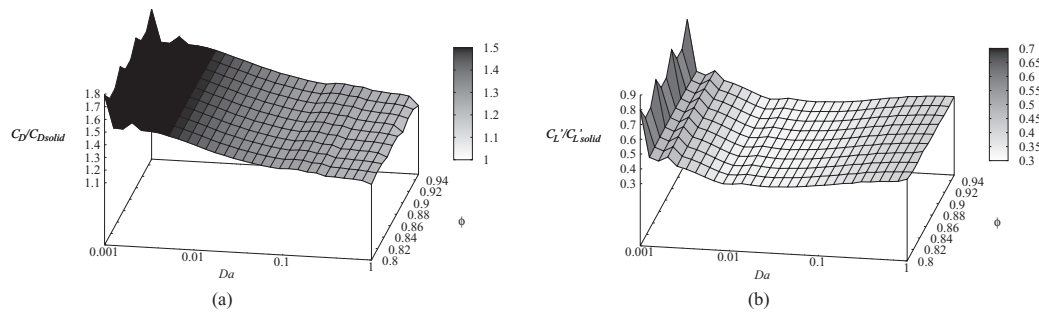
FIG. 4. Mean drag and lift fluctuations $\overline{C_D}$ and $C_L'$ normalized by the values of solid case, computed under different values of Darcy number $Da$ and dimensionless particle diameter $d_p$ ($Re = 1000$, $d = 0.5R$, 2D simulation): (a) $\overline{C_D}$; (b) $C_L'$.

where $F_x$ and $F_y$ denote the force components in the streamwise and the perpendicular directions, respectively. The force acting on the cylinder $\boldsymbol{F}$ is calculated by integrating Eq. (3):

$$\boldsymbol{F} = \oint_{\partial\Omega} p\boldsymbol{n}ds + \oint_{\partial\Omega} \boldsymbol{\tau} \cdot \boldsymbol{n}ds + \int_{\Omega} \boldsymbol{K}dv, \tag{7}$$

where $\boldsymbol{n}$ is the unit vector normal to the porous surface $\partial\Omega$. The first and second terms are the pressure and viscous contributions; the third term is an additional contribution due to the resistance in the porous media.

Figure 4 shows the results of parametric study. Both the mean drag and lift fluctuations are more sensitive to the Darcy number than the porosity. This is simply due to the difference in the parameter ranges considered here: while $Da$ is varied in three decades, $\phi$ is always on the same order of magnitude.

It is also observed that in all cases, $\overline{C_D}$ is increased and $C_L'$ is decreased as compared to the solid case. Within the present parameter range, the maximum suppression of lift fluctuations (i.e., 78% reduction) is obtained in the case of $Da = 2.0 \times 10^{-2}$ and $\phi = 0.95$. Since our main focus is the suppression of lift fluctuations, which is closely related to noise reduction, we select these values to be used in the study presented in Secs. IV–VI.

## IV. FLOW MODIFICATION AT $Re = 1000$

At $Re = 1000$, the boundary layer is laminar, but the wake is three-dimensional.[28] Here, we present the flow modification by porous media at $Re = 1000$ obtained by three-dimensional simulations. The thickness of porous layer is either 20% (Case A) or 50% (Case B) of the total cylinder radius $R$.

### A. Instantaneous field

Before investigating the modification in detail, we present some instantaneous fields to quickly overview how the flow field is modified by the porous media.

Figure 5 shows an instantaneous three-dimensional vortical structure in each case. In the solid case, developing shear layer in the vicinity of the surface shows complex three-dimensionality and the wake region is strongly disturbed. Such three-dimensionality is suppressed in the porous cases, especially in Case B; namely, vortex shedding is more synchronized in the spanwise direction.

An instantaneous field of spanwise vorticity,

$$\omega_z = \frac{\partial v}{\partial x} - \frac{\partial u}{\partial y} = \frac{1}{r}\frac{\partial(ru_\theta)}{\partial r} - \frac{1}{r}\frac{\partial u_r}{\partial \theta}, \tag{8}$$

in a cross-section is depicted in Fig. 6. It is obvious that the shear in the vicinity of cylinder is relaxed by the porous layer and the spanwise vorticity in the near wake is weakened. The small-scale structure due to streamwise vortices observed in the solid case is also suppressed in the porous case,
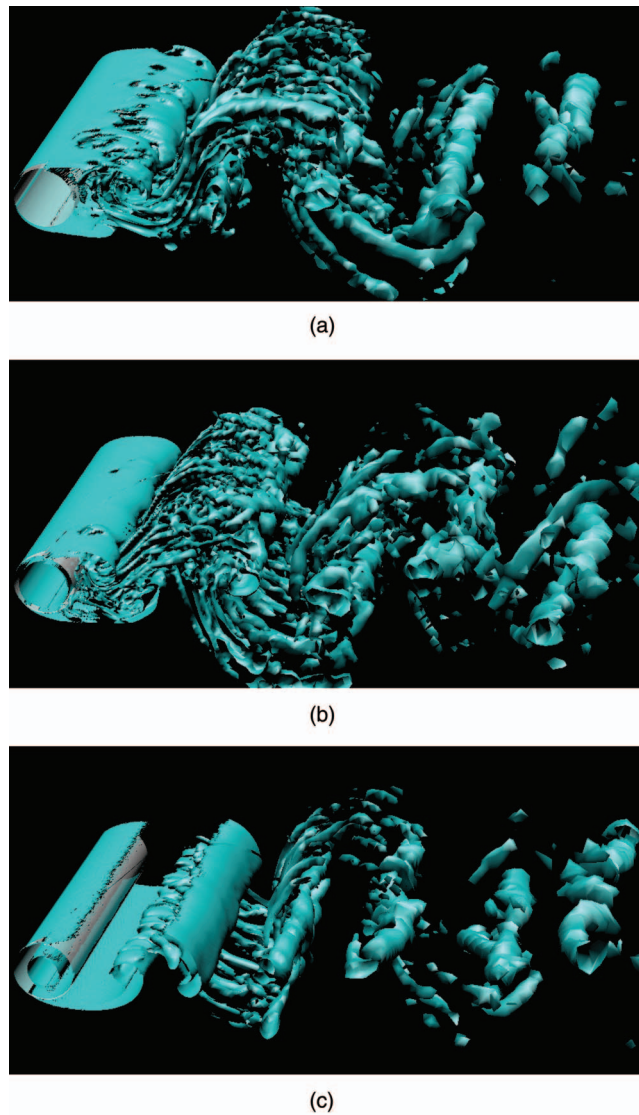
FIG. 5.  Vortical structure ($Re = 1000$, 3D DNS), $\|\boldsymbol{\Omega}\|^2 - \|\boldsymbol{S}\|^2 = 0.8$: (a) solid case; (b) Case A; (c) Case B.

which confirms that the vortex shedding in the porous case is more two dimensional than that in the solid case.

An instantaneous pressure field at the same time instant as Fig. 6 is shown in Fig. 7. It indicates that the pressure gradient near the stagnation point is reduced in the porous case due to the non-zero
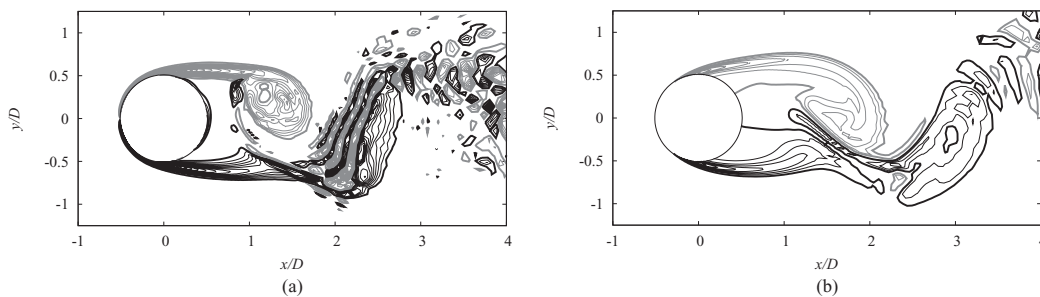


FIG. 6.  Instantaneous vorticity field, ($Re = 1000$, 3D DNS): (a) solid case; (b) Case B. Contour lines: $-15 \leq \omega_z \leq 15$ with increment of 0.6; black, $\omega_z > 0$; gray, $\omega_z < 0$; thick lines, $\omega_z = \pm 0.6$.
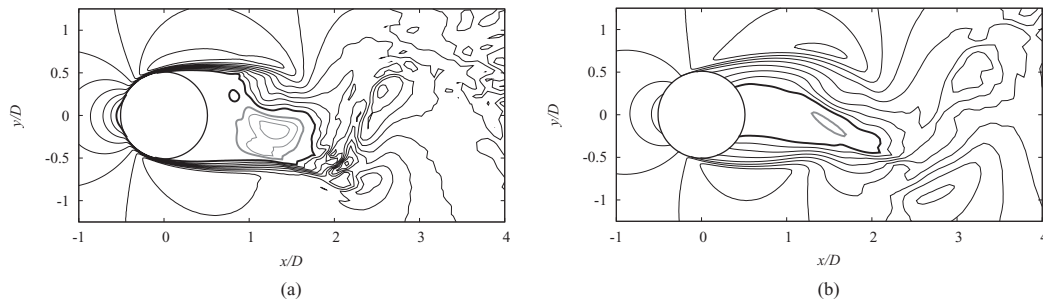
FIG. 7. Instantaneous pressure field, ($Re = 1000$, 3D DNS): (a) solid case; (b) Case B. Contour lines: $-1.5 \leq p \leq 1.5$ with increment of 0.15; black, $p > 0$; gray, $p < 0$; thick lines, $p = \pm 0.15$.

velocity on the porous surface. The pressure gradient in the shear layer and the pressure drop in the wake are also apparently weakened.

## B. Drag, lift, and flow near the surface

Figure 8 shows the time traces of drag and lift coefficients. The time $t$ is made dimensionless by using $U_\infty$ and $D$, and $t = 0$ denotes an instant after the flow reaches its statistically steady state. The drag is increased in both Case A and Case B. On the other hand, the lift force fluctuation is increased in Case A and slightly decreased in Case B. The mean drag ($\overline{C_D}$) in each case is 1.09 (Solid), 1.68 (Case A) and 1.90 (Case B), and the RMS lift fluctuations ($C_L'$) is 0.21 (Solid), 0.39 (Case A) and 0.17 (Case B), respectively. The reduction rate in $C_L'$ (i.e., 19% in Case B) is much smaller than that observed in the two-dimensional simulation (i.e., 78%) presented in Sec. III. In the two-dimensional simulation, the vortex shedding is, of course, always synchronized in the spanwise direction; thus, $C_L'$ is directly related to the "local" lift force fluctuations. In contrast, in the three-dimensional case, the vortex shedding at different spanwise locations has phase difference; thus, $C_L'$, which is averaged over the span, is much smaller than the amplitude of local lift force fluctuations at a single spanwise location. When the porous medium is applied, the vortex shedding becomes more two-dimensional as observed above, which works to increase $C_L'$; at the same time the shed vortex becomes weaker, which works to reduce $C_L'$. The larger reduction rate obtained in the two-dimensional simulation can thus be explained by the absence of the former effect to increase $C_L'$.

Figure 9 shows different constitutions to the total drag: the pressure contribution $C_{Dp}$, the frictional contribution $C_{Df}$, and the drag inside the porous media $C_{Dk}$. In all cases, $C_{Dp}$ is dominant and $C_{Df}$ is much smaller than the other components; $C_{Df}$ becomes even smaller in porous cases. For thicker porous layer, $C_{Dk}$ becomes larger: in Case B, $C_{Dk}$ amounts to 30% of the total drag.
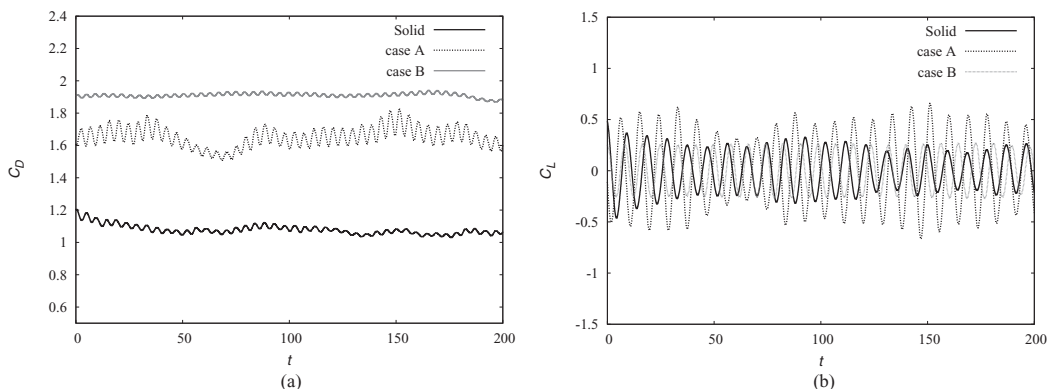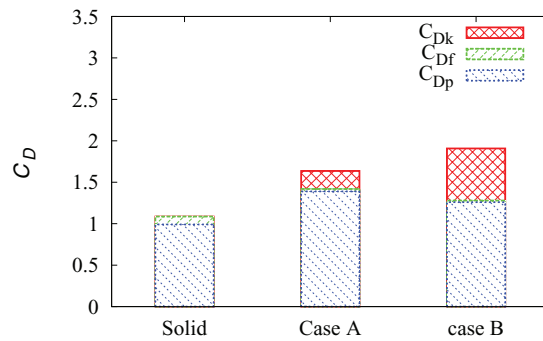


FIG. 8. Time traces of drag and lift coefficients ($Re = 1000$, 3D DNS): (a) drag coefficient $C_D$; (b) lift coefficient $C_L$.

FIG. 9.  Composition of mean drag coefficient ($Re = 1000$, 3D DNS).

Figures 10(a) and 10(b) show the distributions of the pressure coefficient $C_p$ and the friction coefficient $C_f$ on the cylinder surface, defined, respectively, as

$$C_p = \frac{\overline{p}_w - p_\infty}{\frac{1}{2}\rho U_\infty^2}\,, \qquad C_f = \frac{\tau_w}{\frac{1}{2}\rho U_\infty^2},$$

(9)

where $\overline{p}_w$, $p_\infty$, and $\tau_w$ denote the mean wall pressure, the free-stream pressure, and the mean wall-shear stress, respectively. The stagnation pressure is found to be lower than unity in porous cases due to the non-zero velocity on the porous surface. The lower pressure in Case B suggests that the velocity at the stagnation point is higher than that in Case A. Although the pressure distribution on a solid cylinder usually has a local minimum point in the Reynolds number range studied here, as can be found in literature (e.g., Ref. 28), such a local minimum is absent in the porous cases. The
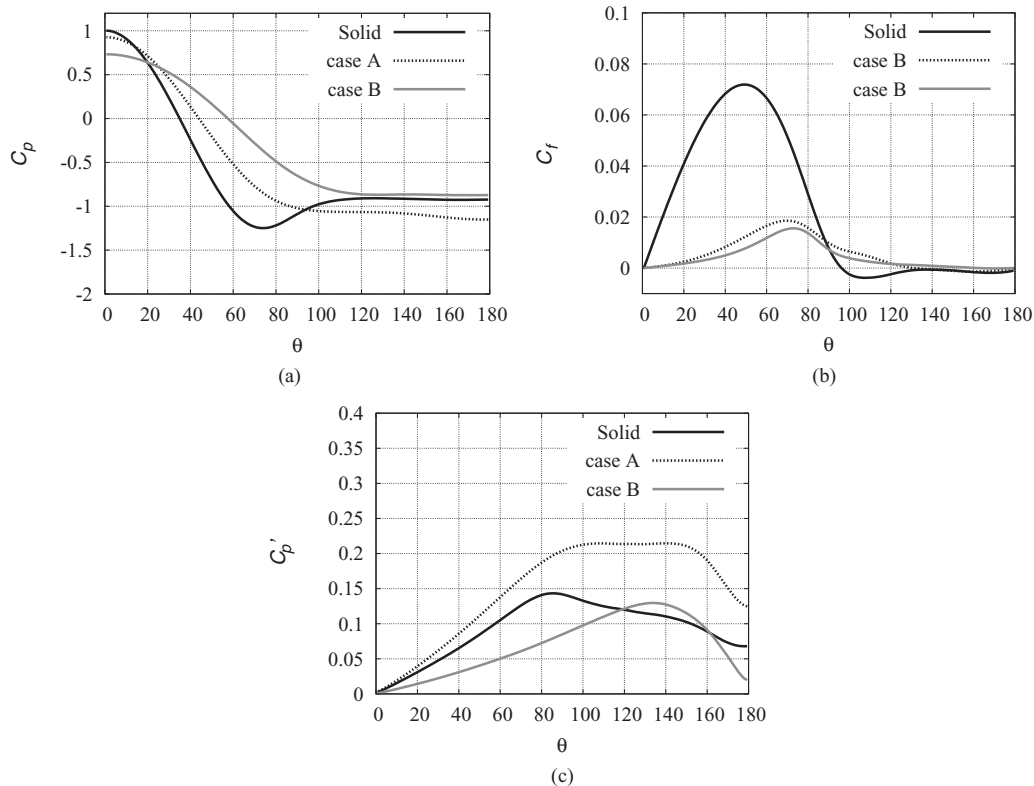


FIG. 10.  Local force distribution on the surface ($Re = 1000$, 3D DNS): (a) pressure coefficient ($C_p$); (b) friction coefficient ($C_f$); (c) RMS of pressure coefficient ($C_p'$).
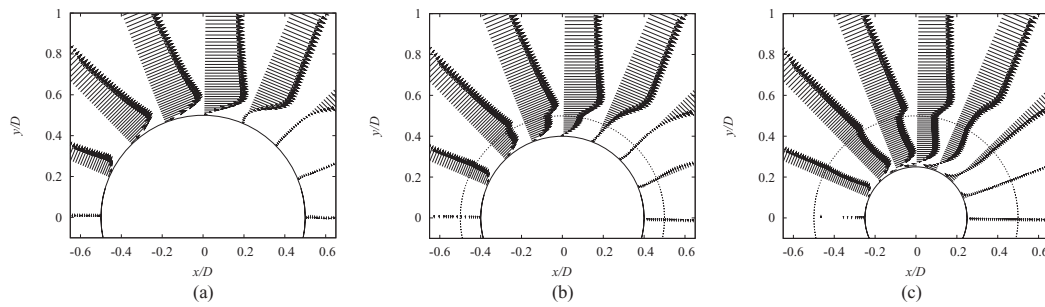
FIG. 11. Mean circumferential velocity profiles ($Re = 1000$, 3D DNS): (a) solid case; (b) Case A; (c) Case B. Solid line, surface of solid cylinder; dotted line, porous surface.

higher pressure on the front side ($40° \leq \theta \leq 80°$) results in the increase of $C_{Dp}$ of porous cases. The smaller $C_{Dp}$ in Case B than Case A is due to the higher pressure on the rear side ($100° \leq \theta \leq 180°$). As for the friction, $C_f$ in the porous cases is much smaller than that in the solid case due to the slip velocity on the porous surface.

The distribution of RMS pressure coefficient $C'_p$, defined as

$$C'_p = \frac{\sqrt{\overline{p'^2}}}{\frac{1}{2}\rho U_\infty^2}$$                    (10)

is shown in Fig. 10(c). The pressure fluctuation is increased in Case A and decreased in Case B. Although the local maximum in Case B has a magnitude comparable to that in the solid case, its location is shifted backward. Because the lift force is calculated by $\int p \sin\theta d\theta$, such backward shift leads to the suppression of the lift fluctuation.

Figure 11 illustrates the mean azimuthal velocity profiles near the cylinder surface. It is clear that the surface velocity is non-zero in Cases A and B. Due to this slip velocity, the friction on the porous surface is reduced as observed in Fig. 10(b). The azimuthal velocity inside the porous media of Case B looks "fully developed" away from the wall and back flow is observed near the solid surface. In contrast, Case A shows spatially developing azimuthal velocity profiles with a smaller amount of back flow. The velocity distribution indicates that the flux in the porous media is larger in Case B.

Figure 12 shows the distribution of mean wall-normal velocity on the porous surface. The fluid is sucked in the front half, which reduces the pressure at the stagnation point as observed in Fig. 10(b), and blown in the rear half. The outward wall-normal velocity takes its maximum value around $92°$ in Case A and $113°$ in Case B.
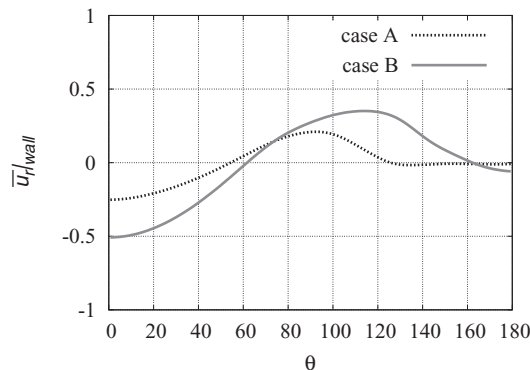


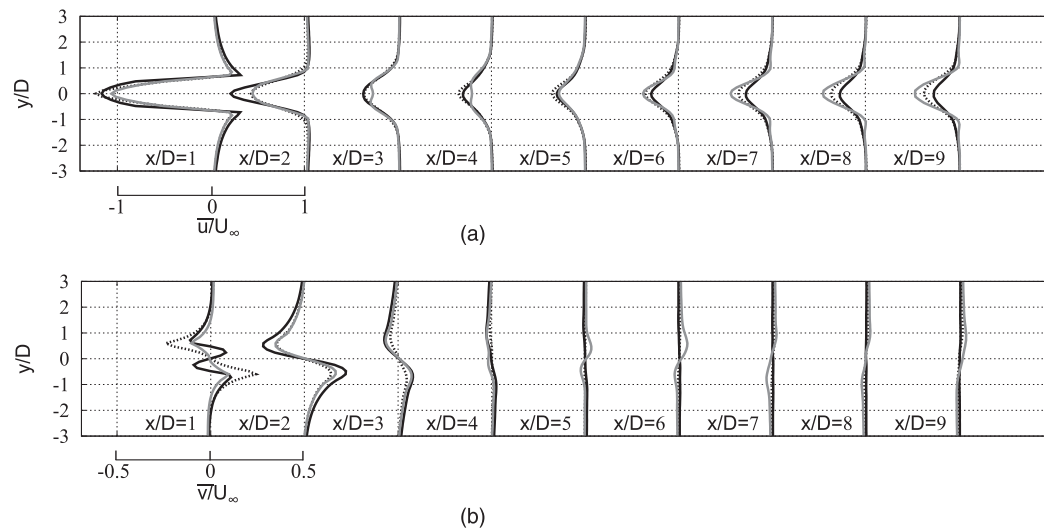FIG. 12. Mean wall-normal velocity on the porous surface ($Re = 1000$, 3D DNS).

FIG. 13. Mean velocity profiles ($Re = 1000$, 3D DNS): (a) mean streamwise velocity; (b) mean lateral velocity. Black solid line, solid case; black dotted line, Case A; gray solid line, Case B.

## C. Statistics in the downstream wake

Figure 13(a) shows the mean streamwise velocity in the downstream wake. The momentum deficit in the porous case is smaller than that in the solid case in the near wake, but larger in the far wake. The smaller deficit in the near wake is the direct consequence of modification near the surface observed above. However, the increase of deficit in the far wake cannot be explained simply by the modification near the surface. According to the mean pressure distribution in the downstream wake, as shown in Fig. 14, the mean pressure field is found to be modified globally; in particular, the mean streamwise pressure gradient the porous case is increased in the region of $6 < x/D < 10$ as compared to the solid case. This larger pressure gradient is considered to cause the larger momentum deficit in the far wake (Fig. 13(a)) through the acceleration of flow toward the upstream direction.

The mean lateral velocity, shown in Fig. 13(b), is largely modified at $x/D = 1$. This can be attributed to the change in the length of recirculation region, as will be shown below (Fig. 15). Although the lateral velocity is considerably smaller than the streamwise velocity, slightly stronger
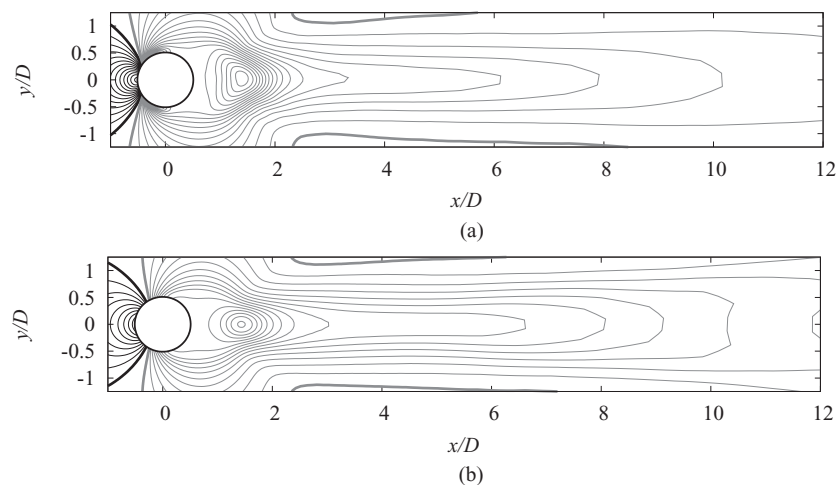


FIG. 14. Mean pressure field ($Re = 1000$, 3D DNS): (a) solid case; (b) Case B. Contour lines: $-1.5 \leq \overline{p} \leq 1.5$ with increment of 0.075; black, $\overline{p} > 0$; gray, $\overline{p} < 0$; thick lines, $\overline{p} = \pm 0.075$.
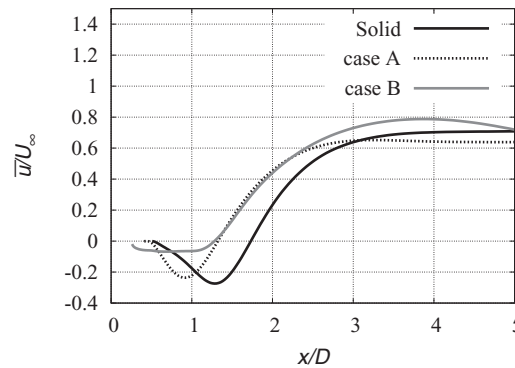
FIG. 15.  Mean streamwise velocity on the centerline, i.e., $y/D = 0$ ($Re = 1000$, 3D DNS).

outward motion in the far wake can be noticed in the porous case. Note that some dissymmetry observed in the far wake seems to be due to the insufficient integration time. We have performed computation with twice as long integration time ($TU_\infty/D = 400$) as the original one ($TU_\infty/D = 200$), but dissymmetry was still observable. Since the value of mean lateral velocity itself is very small in the far wake, an extraordinarily long integration time may be needed in order to obtain a profile, which looks completely antisymmetric.

Figure 15 shows the mean streamwise velocity on the centerline. Compared to the solid case, the recirculation region is found to be shortened in the porous cases; moreover, the velocity inside the recirculation region is much reduced in Case B. Recall that the mean lateral velocity is largely modified at $x/D = 1$. At that location, the velocity gradient $\partial \overline{u}/\partial x$ is negative in solid case, positive in Case A, and slightly positive in Case B. Due to the continuity, $\partial \overline{v}/\partial y$ takes the sign opposite to $\partial \overline{u}/\partial x$, which is consistent with the observations in Fig. 13 (b). In contrast, at $x/D = 2$, i.e., downstream of the recirculation region, $\partial \overline{u}/\partial x$ is positive in all cases with a similar magnitude. Therefore, the difference in lateral velocity profiles is small. Similarly, the positive $\partial \overline{v}/\partial y|_{y=0}$ observed in the far wake of Case B can be explained by the increase of streamwise momentum deficit, i.e., $\partial \overline{u}/\partial x < 0$ in the region of $x/D > 4$.

In order to discuss the modification from the viewpoint of vorticity, the RMS vorticity distributions at different locations are shown in Fig. 16. The spanwise vorticity $\omega_z$ is generated on the cylinder surface; therefore, $\omega_{z,rms} = \sqrt{\overline{\omega_z'^2}}$ is large near the cylinder and gradually smoothed in the downstream. On the other hand, the streamwise vorticity $\omega_x = \partial w/\partial y - \partial v/\partial z$ is generated by the reorientation from the spanwise vorticity $\omega_z$; thus, the maximum value of $\omega_{x,rms} = \sqrt{\overline{\omega_x'^2}}$ is found at a bit downstream. The spanwise vorticity of porous case is smaller than that of the solid case due to the slip-velocity on the porous surface, while the profiles nearly collapse in the downstream region, $x/D \geq 4$. Observing the smaller streamwise vorticity in the porous case, the slightly higher value of $\omega_{z,rms}$ in the far wake of the porous case can be attributed to the smaller amount of reorientation of spanwise vortices to the streamwise ones.

## V. REYNOLDS NUMBER DEPENDENCY

So far, we have discussed the effects of porous media at a fixed Reynolds number, i.e., $Re = 1000$. In this section, we investigate the dependency of porous media effect on the Reynolds number. We present the results at: $Re = 100$, where the wake is completely two-dimensional; $Re = 3900$, a higher Reynolds number, at which previous studies are available for comparison; and $Re = 1.0 \times 10^5$, which is close to the Reynolds number in the experimental study by Sueki *et al.*[2]

The drag coefficient $\overline{C_D}$ and the RMS lift coefficient $C_L'$ are shown in Table IV and their ratios to the solid values are plotted in Fig. 17 as functions of Reynolds number. Except for the two-dimensional regime, i.e., $Re = 100$, the amount of drag increase becomes smaller with the Reynolds number. The drag increase in Case B is larger than Case A at lower Reynolds number and smaller
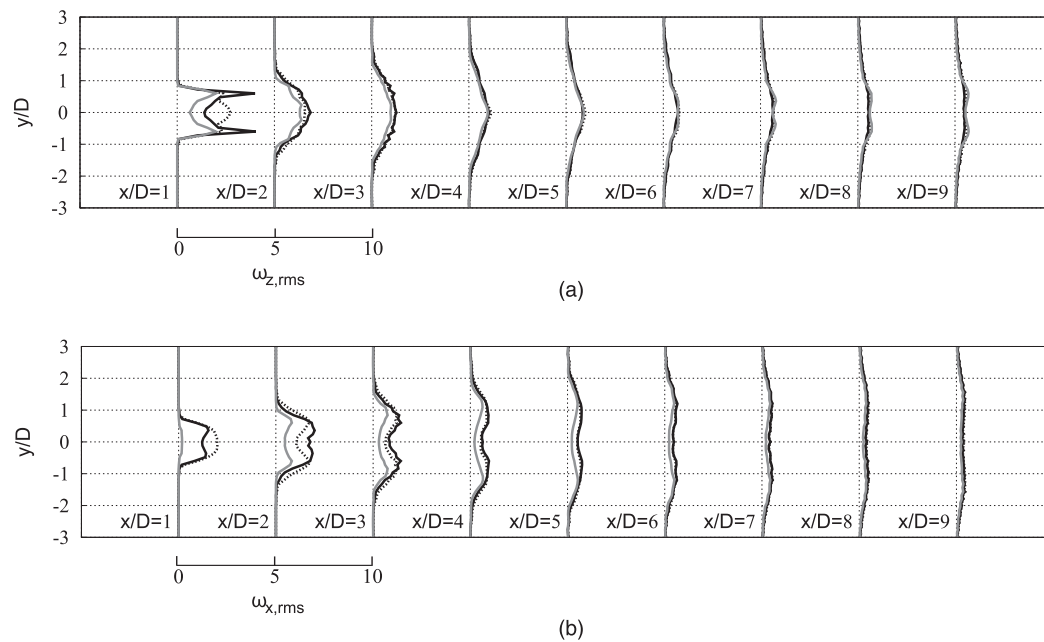
FIG. 16.  RMS vorticity: (a) spanwise component; (b) streamwise component ($Re = 1000$, 3D DNS). Black solid line, solid case; black dotted line, Case A; gray solid line, Case B.

at higher Reynolds number. The lift fluctuations also decrease with Reynolds number except for Case A in the two-dimensional regime. The high value of $C'_L$ at $Re = 1000$ can be attributed to the spanwise synchronization of vortex shedding as discussed above. The reduction of $C'_L$ is more effective at higher Reynolds number and the lift fluctuation is completely suppressed at $Re = 1.0 \times 10^5$ in Case B.

Figure 18 shows instantaneous vorticity fields at $Re = 1.0 \times 10^5$. In the porous case (Case B), the vortex shedding is completely suppressed and the shear layers are nearly symmetric. This is similar to the experimental observation of Sueki et al.[2] (Fig. 1(b)).

The power spectral density (PSD) of lift coefficient $C'_L$ in each case is compared in Fig. 19 together with that in literature (Schewe,[26] $Re = 1.3 \times 10^5$). Although the Reynolds numbers are slightly different, the Strouhal number in the present solid case, i.e., $St = fD/U_\infty = 0.18$, is in fair agreement with that of Schewe's, i.e., $St = 0.20$. Furthermore, the shape near the peak is similar:

TABLE IV.  Reynolds number dependency of the computed flow properties.

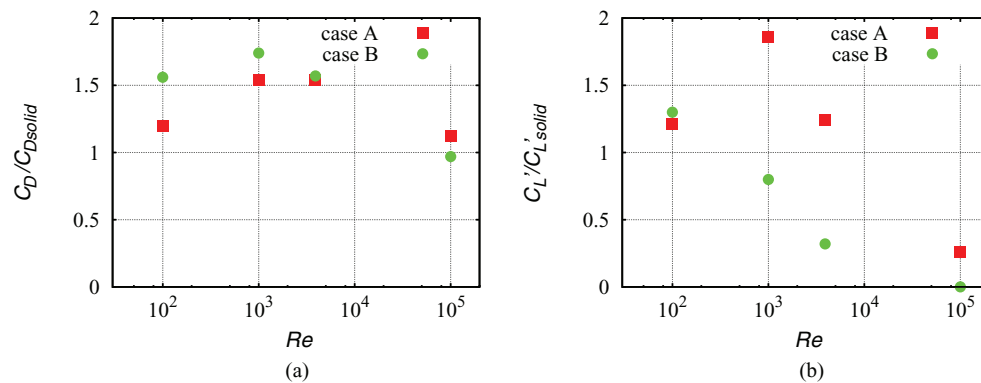| Reynolds number | Surface | $\overline{C_D}$ | $C'_L$ |
|---|---|---|---|
| $Re = 100$ | Solid | 1.33 | 0.23 |
| | Case A | 1.59 | 0.28 |
| | Case B | 2.07 | 0.30 |
| $Re = 1000$ | Solid | 1.09 | 0.21 |
| | Case A | 1.68 | 0.39 |
| | Case B | 1.90 | 0.17 |
| $Re = 3900$ | Solid | 1.07 | 0.25 |
| | Case A | 1.65 | 0.31 |
| | Case B | 1.69 | 0.08 |
| $Re = 1.0 \times 10^5$ | Solid | 1.46 | 0.99 |
| | Case A | 1.63 | 0.26 |
| | Case B | 1.42 | 0.00 |

FIG. 17.   Reynolds number dependency: (a) mean drag coefficient $\overline{C_D}$; (b) RMS of lift coefficient $C'_L$.

the slope in the low frequency side is slow and that in the high frequency side is steep. The result of Schewe has another small energy peak near $St = 0.6$, which is not present in our result. This peak seems to correspond to the eigenfrequency of the balance used for the force measurement, i.e., 385 Hz, which is reported in their paper. Modification by the porous surfaces can be clearly observed. In Case A, the power is significantly reduced and the Strouhal number is slightly increased. In Case B, the power is nearly zero over all frequencies, which confirms that the lift fluctuation is completely suppressed.

Figure 20 shows the mean surface pressure distribution at different Reynolds numbers. As has been observed in Sec. IV, the porous surface removes the local minimum and flatten the distribution. At $Re = 100$, the modification is similar to, but much weaker than that at $Re = 1000$ (Fig. 10(a)). At $Re = 3900$, the distribution is more flattened and the base pressure $C_{pb}$ in Case B is even higher than that at lower Reynolds number. At $Re = 1.0 \times 10^5$, the pressure distribution becomes even more flattened.

Figure 20 also compares the RMS surface pressure fluctuations at different Reynolds numbers. The modification at $Re = 100$ is similar to, but weaker than that observed at $Re = 1000$ (Fig. 10(c)). The pressure fluctuation becomes smaller at higher Reynolds number, and eventually almost vanishes at $Re = 1.0 \times 10^5$ (Case B).

## VI. MECHANISM OF FLOW MODIFICATION

We have observed in Sec. IV that several quantities closely related to flow oscillations in the downstream wake, such as wall-shear, surface pressure fluctuations, and resultant lift fluctuations are suppressed by porous surface. In Sec. V, we have also seen that the effect becomes more significant at higher Reynolds numbers and with thicker porous layer. Here, we attempt to consistently explain
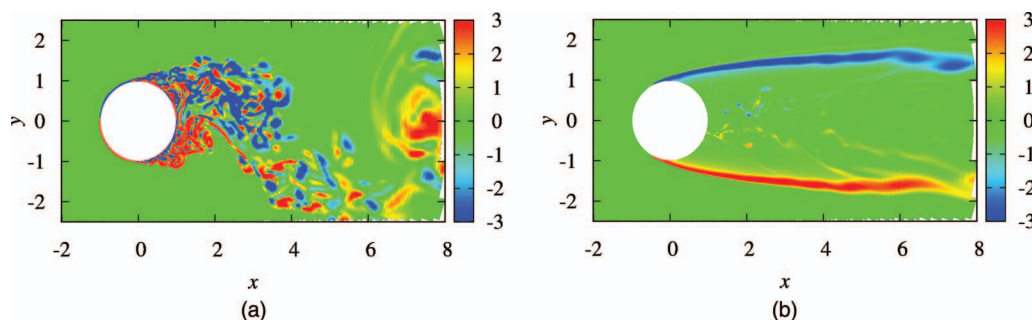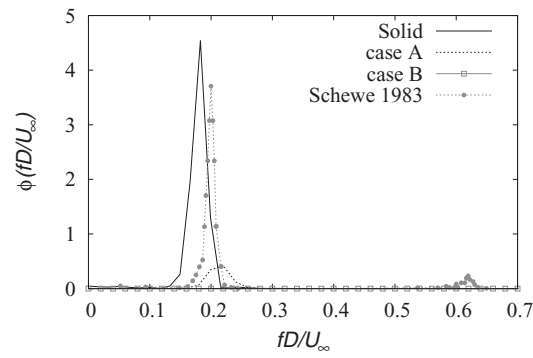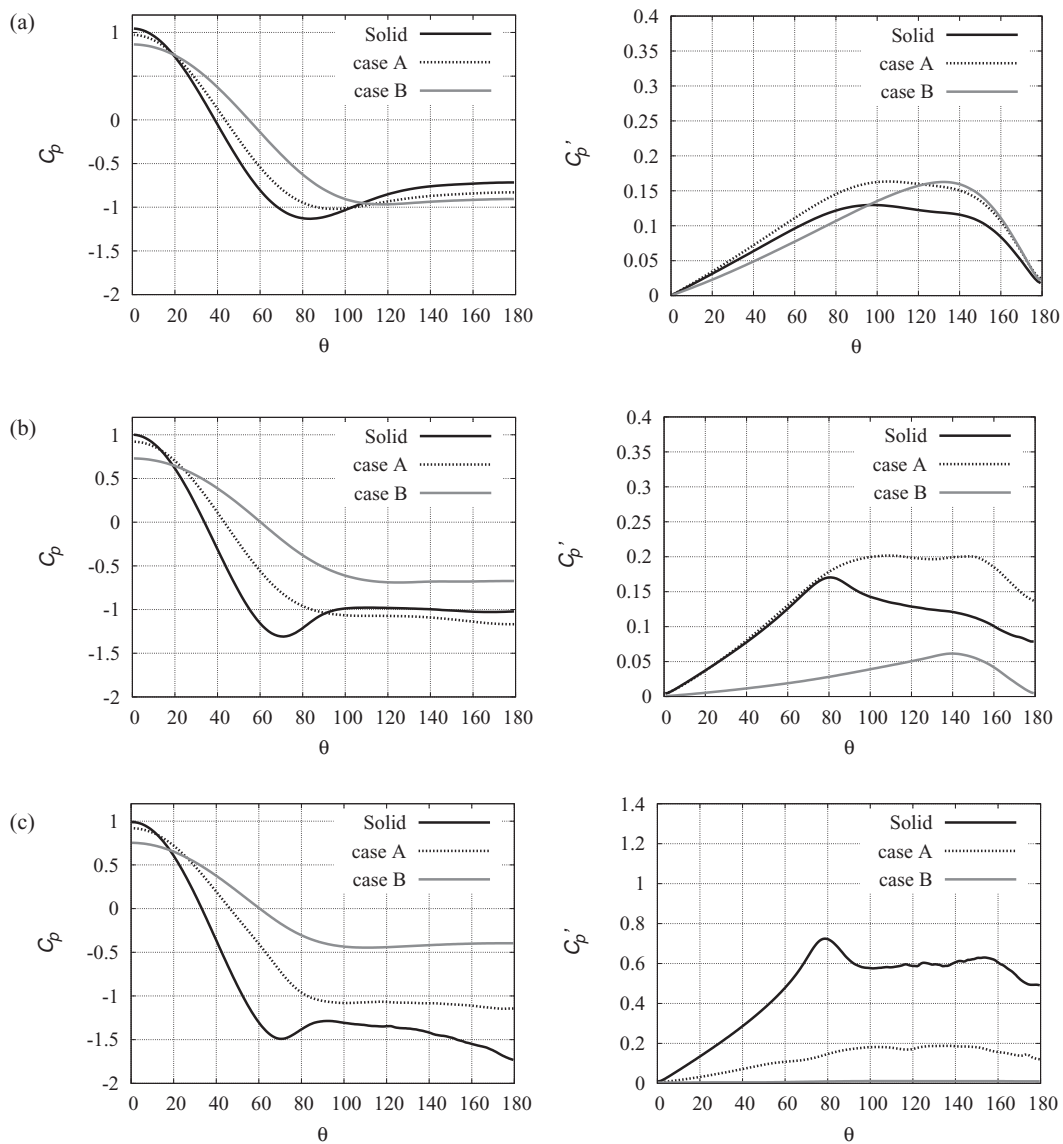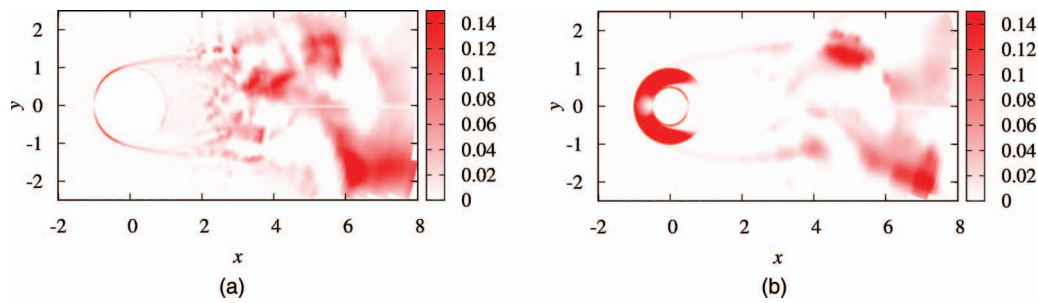


FIG. 18.   Instantaneous vorticity field ($Re = 1.0 \times 10^5$, LES): (a) solid case; (b) Case B.

FIG. 19.  Power spectral density of lift fluctuations ($Re = 1.0 \times 10^5$).



FIG. 20.  Mean ($\overline{C_p}$, left) and RMS ($C_p'$, right) pressure coefficients on the cylinder surface: (a) $Re = 100$; (b) $Re = 3900$; (c) $Re = 1.0 \times 10^5$.

FIG. 21. Energy dissipation $\varepsilon$ at $Re = 3900$ (LES): (a) solid case; (b) Case B.

the mechanism of flow modification from two aspects: the dissipation of kinetic energy and the slip velocity on the porous surface.

The dissipation outside the cylinder is expressed as

$$\varepsilon = \frac{\|\nabla \boldsymbol{u}\|^2}{Re} \tag{11}$$

in the non-dimensional form. The dissipation inside the porous media is easily obtained by multiplying the macroscopic velocity $\langle \boldsymbol{u} \rangle$ to Eq. (3) as

$$\varepsilon = \frac{\|\nabla \langle \boldsymbol{u} \rangle \|^2}{Re} + \langle \boldsymbol{u} \rangle \cdot \boldsymbol{K}, \tag{12}$$

where the second term accounts for the internal friction.

Figure 21 shows the instantaneous energy dissipation fields at $Re = 3900$. Dissipation in the porous media is found to be extremely large as compared to that in the boundary layer, detached shear layer, and wake. By this energy dissipation process, the fluid that passes through the porous media loses a large amount of its energy before being ejected from the downstream side. The fluid constantly ejected from the porous surface forms a stable low-energy (low-speed and low-pressure) fluid region.

In Sec. III, we have seen that the shear and vorticity on the surface are weakened by the slip velocity. That means, the detached eddies destabilizing the flow are also weakened.

These two mechanisms consistently explain the dependencies mentioned above. The Reynolds number dependency can be explained by the diffusivity. At lower Reynolds number, the low energy fluids ejected from the porous surface is immediately diffused to wider area and convected away by high-speed flows. At higher Reynolds number, in contrast, the ejected low-energy fluid forms a large low-energy fluid region before diffusing. Note that the turbulent diffusion is also considered to be suppressed in the stabilized wake. Thus, the porous medium works better at higher Reynolds number.

Figure 22 shows the distribution of total pressure coefficient (i.e., a pressure coefficient built on the total pressure $p_t = p + \rho \boldsymbol{u}^2/2$) in the solid case and Case B at different Reynolds numbers. Although the difference between the solid and porous cases is small at $Re = 100$, a stronger low pressure area can be observed in porous cases. The difference becomes clearer as the Reynolds number increases. At $Re = 3900$, a very low energy region is observed in the solid case, while it is recovered in Case B. This recovery is likely due to the low energy fluid ejected from the porous surface. At $Re = 1.0 \times 10^5$, the low energy region in the porous case is expanded further downstream.

As for the dependency to the porous media thickness, we have seen that the mass flow rate inside the porous media is larger for thicker porous layer. As a result of this, the amount of low-energy fluid ejected from the porous surface and the low-energy region in the wake become larger.

One might consider that the effect is similar to so-called base bleeding. The above-mentioned mechanisms, however, are not the same as the case of base bleeding. In order to demonstrate it, we conducted a numerical simulation of a solid case, but with the mean radial velocity on the surface obtained in Case B. The Reynolds number is 3900. This condition mimics the porous surface but does not account for the slip velocity and the energy dissipation inside the porous media. The
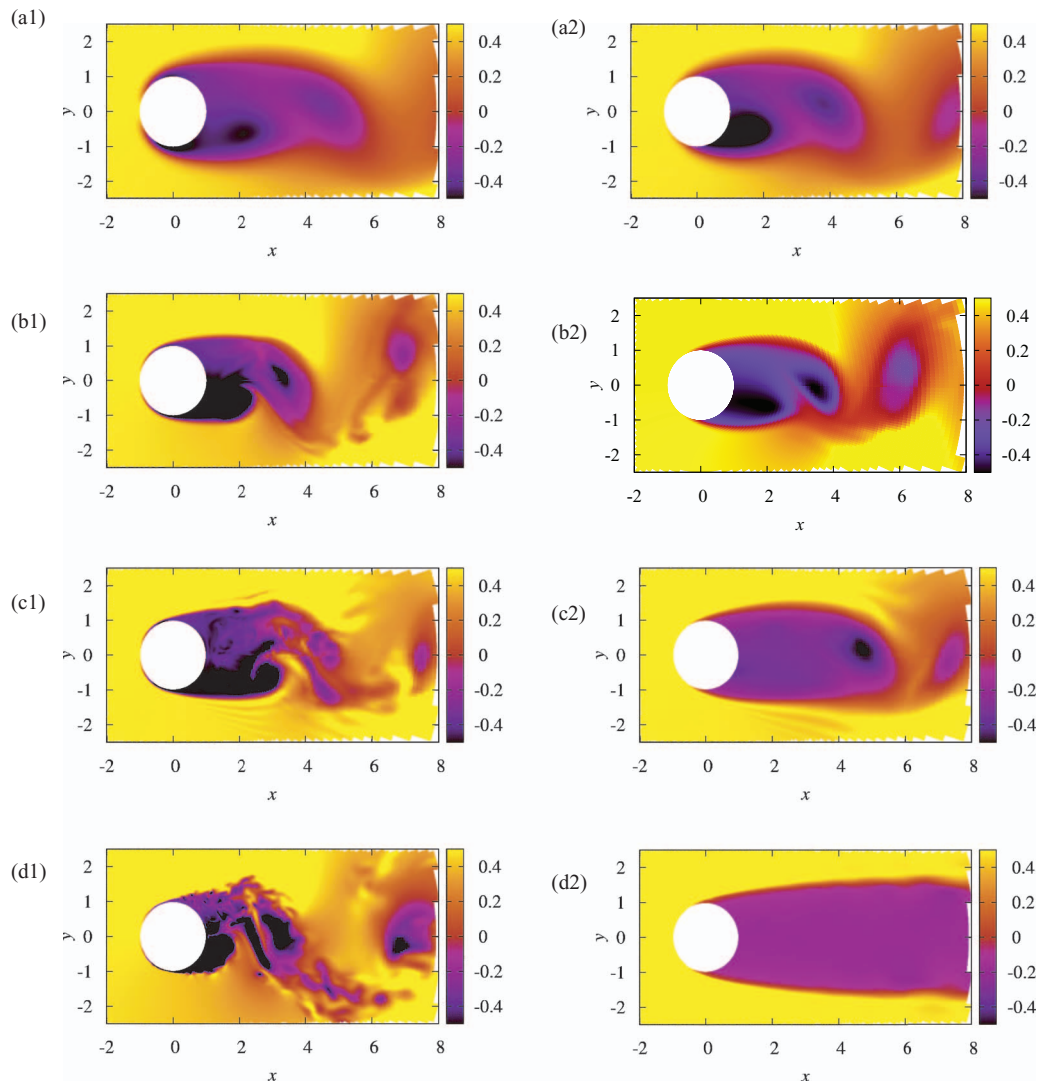
FIG. 22. Instantaneous distribution of total pressure coefficient (a) $Re = 100$; (b) $Re = 1000$; (c) $Re = 3900$; (d) $Re = 1.0 \times 10^5$. (a1)-(d1) solid case; (a2)-(d2) Case B.

computed drag coefficient is 1.36 and the RMS of lift coefficient is 0.27. The $C'_L$ is rather increased in contrast to the huge suppression in Case B. Figure 23 shows the instantaneous vorticity field. The flow structure is apparently different from Case B: for instance, the shear region is spread to lateral direction. This result implies that the slip velocity on the porous surface and the energy dissipation process play very important role for the flow modification by the porous media.

## VII. SUMMARY AND CONCLUSIONS

Flow around a circular cylinder having porous surface of uniform thickness, permeability, and porosity has been investigated by the means of DNS and LES. Parametric study using two-dimensional computation at $Re = 1000$ defines the most effective set of porous media properties. With these properties, a detailed flow modification is studied at $Re = 100$, 1000, 3900, and $1.0 \times 10^5$. The porous surface is found to increase the drag regardless of the Reynolds number: the drag increase is more pronounced at lower Reynolds number. On the other hand, the porous surface has an effect to suppress the lift fluctuation: the effect is larger at higher Reynolds number.
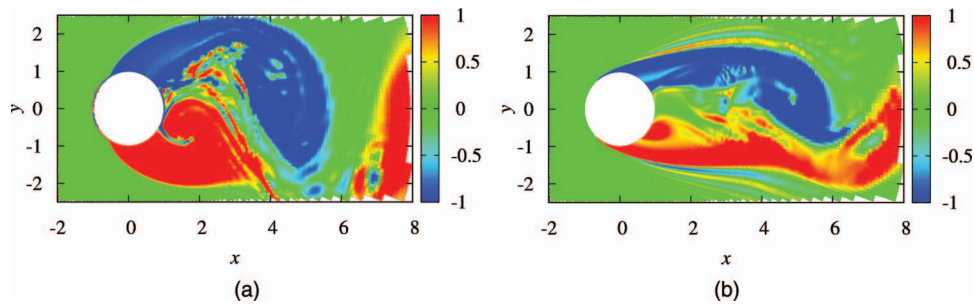
FIG. 23.  Vorticity distribution at $Re = 3900$ (LES): (a) solid case with wall-normal velocity; (b) Case B.

At $Re = 1000$, it is shown that the unsteadiness of the flow field is suppressed by the porous media: the surface pressure fluctuation is suppressed and the vortical structure of shear layer becomes more two-dimensional as compared to the fully three-dimensional structure in the solid case. Such stabilization effect is found to be clearer at higher Reynolds number. Particularly, at $Re = 1.0 \times 10^5$ the RMS of lift coefficient nearly vanishes and the flow field becomes symmetric as has been observed in the experimental study of Sueki *et al.*[2]

These flow modifications are explained in terms of slip velocity and fluid energy. The shear and the vorticity near the surface are weakened by the slip velocity. The fluid that enters into the porous media loses its energy due to strong dissipation and the resultant low-energy fluid is ejected from the downstream side of the porous surface. A stable shear layer is likely to be formed by the combination of these two effects.

In the present study, we investigated only four different Reynolds numbers: the case at $Re = 100$ represents the two-dimensional laminar flow regime, and other three cases at $Re = 1000$, 3900, and $1.0 \times 10^5$ are all in the subcritical regime. From the present results, however, we can at least conjecture the following effects at higher Reynolds numbers. First, the growth of instability in the boundary and shear layers would be delayed by the porous surface; hence the critical Reynolds number for laminar-to-turbulent transition would be shifted up. Even in the fully turbulent regime, the wide low energy region would be created in the wake and the fluctuations of flow field would be eliminated. As for the thickness of porous layer, we studied two different thicknesses and found that the thicker porous layer is more effective in reducing the lift fluctuations. However, an important question is still open: "What is the critical thickness to eliminate the lift fluctuations?" More detailed investigation on the dependency on the Reynolds number and the thickness of porous layer is left as future work.

## ACKNOWLEDGMENTS

[1] H. Choi, W.-P. Jeon, and J. Kim, "Control of flow over a bluff body," Annu. Rev. Fluid Mech. **40**, 113 (2008).
[2] K. Sueki, T. Takaishi, and M. Ikeda, "Application of porous material to reduce aerodynamic sound from bluff bodies," Fluid Dyn. Res. **42**, 015004 (2010).
[3] C.-H. Bruneau and I. Mortazavi, "Passive control of the flow around a square cylinder using porous media," Int. J. Numer. Methods Fluids **46**, 415 (2004).
[4] C.-H. Bruneau and I. Mortazavi, "Control of vortex shedding around a pipe section using a porous sheath," Int. J. Offshore Polar Eng. **16**, 90 (2006).
[5] N. S. Martys and H. Chen, "Simulation of multicomponent fluids in complex three-dimensional geometries by the lattice Boltzmann method," Phys. Rev. E **53**, 743 (1996).
[6] J. Jiménez, M. Uhlmann, A. Pinelli, and G. Kawahara, "Turbulent shear flow over active and passive porous surfaces," J. Fluid Mech. **442**, 89 (2001).
[7] C. T. Hsu and P. Cheng, "Thermal dispersion in porous medium," Int. J. Heat Mass Transfer **33**, 1587 (1990).
[8] S. Ergun, "Fluid flow through packed columns," Chem. Eng. Prog. **48**, 89 (1952).

[9] M. Germano, U. Piomelli, P. Moin, and C. H. William, "A dynamic subgrid-scale eddy viscosity model," Phys. Fluids A **3**, 1760 (1991).

[10] D. K. Lilly, "A proposed modification of the Germano subgrid-scale closure method," Phys. Fluids A **4**, 633 (1991).

[11] J. Smagorinsky, "General circulation experiments with the primitive equations," Mon. Weather Rev. **91**, 99 (1963).

[12] M. Breuer, "A challenging test case for large eddy simulation: High Reynolds number circular cylinder flow," Int. J. Heat Fluid Flow **21**, 648 (2000).

[13] K. Fukagata and N. Kasagi, "Highly energy-conservative finite difference method for the cylindrical coordinate system," J. Comput. Phys. **181**, 478 (2002).

[14] B. P. Leonard, "A stable and accurate convective modelling procedure based on quadratic upstream interpolation," Comput. Methods Appl. Mech. Eng. **19**, 59 (1979).

[15] P. R. Spalart, R. D. Moser, and M. M. Rogers, "Spectral methods for the Navier-Stokes equations with one infinite and two periodic directions," J. Comput. Phys. **96**, 297 (1991).

[16] J. K. Dukowicz and A. S. Dvinsky, "Approximate factorization as a higher order splitting for the implicit incompressible flow equations," J. Comput. Phys. **102**, 336 (1992).

[17] R. D. Henderson, "Details of the drag curve near the onset of vortex shedding," Phys. Fluids **7**, 2102 (1995).

[18] C. Norberg, "Fluctuating lift on a circular cylinder: Review and new measurements," J. Fluids Struct. **17**, 57 (2003).

[19] C. Norberg, "Flow around a circular cylinder: Aspects of fluctuating lift," J. Fluids Struct. **15**, 459 (2001).

[20] C. H. K. Williamson and A. Roshko, "Measurements of base pressure in the wake of a cylinder at low Reynolds numbers," Z. Flugwiss. Weltraumforsch. **14**, 38 (1990).

[21] R. D. Henderson and G. Karniadakis, "Unstructured spectral element methods for simulation of turbulent flows," J. Comput. Phys. **122**, 191 (1995).

[22] J. H. Gerrard, "A disturbance-sensitive Reynolds number range of the flow past a circular cylinder," J. Fluid. Mech. **22**, 187 (1965).

[23] A. G. Kravchenko and P. Moin, "Numerical studies of flow over a circular cylinder at $Re_D = 3900$," Phys. Fluids **12**, 403 (2000).

[24] J. Kim and H. Choi, "Distributed forcing of flow over a circular cylinder," Phys. Fluids **17**, 033103 (2005).

[25] C. Norberg, "Effects of Reynolds number and a low-intensity freestream turbulence on the flow around a circular cylinder," Publication No. 87/2, Department of Applied Thermodynamics and Fluid Mechanics, Chalmers University of Technology, Sweden, 1987.

[26] G. Schewe, "On the force fluctuations acting on a circular cylinder in crossflow from subcritical up to transcritical Reynolds numbers," J. Fluid. Mech. **133**, 265 (1983).

[27] C. Norberg, "Turbulence and Reynolds number effects on the flow and fluid forces on a single cylinder in cross flow," J. Fluids Struct. **1**, 337 (1987).

[28] M. M. Zdravkovich, *Flow Around a Circular Cylinders: Fundamentals* (Oxford University Press, Oxford, 1997), Vol. 1.